UNIVERSITYOF BIRMINGHAM

Production and dispersion of free radicals from transient cavitation bubbles

Peng, Kewen; Qin, Frank G.F.; Jiang, Runhua; Qu, Wanjun; Wang, Qianxi

Document Version
Publisher's PDF, also known as Version of record

Link to publication on Research at Birmingham portal

Production and dispersion of free radicals from transient cavitation Bubbles: An integrated numerical scheme and applications

Kewen Peng [a],[*], Frank G.F. Qin [a], Runhua Jiang [a], Wanjun Qu [a], Qianxi Wang [b]

[a] *Guangdong Provincial Key Laboratory of Distributed Energy Systems, Dongguan University of Technology, Dongguan 523808, China*
[b] *School of Mathematics, University of Birmingham, Birmingham B15 2TT, United Kingdom*

A B S T R A C T

As an advanced oxidation process with a wide range of applications, sonochemistry relies on acoustic cavitation to induce free radicals for degrading chemical contaminants. The complete process includes two critical steps: the radical production inside the cavitation bubble, and the ensuing dispersion of these radicals into the bulk solution. To grasp the physicochemical details in this process, we developed an integrated numerical scheme with the ability to quantitatively describe the radical production-dispersion behavior. It employs coupled simulations of bubble dynamics, intracavity chemical reactions, and diffusion–reaction-dominated mass transport in aqueous solutions. Applying this method to the typical case of argon and oxygen bubbles, the production mechanism for the main radicals is revealed. Moreover, the temporal-spatial distribution of the radicals in the liquid phase is presented. The results demonstrate that the enhanced radical production observed in oxygen bubbles can be traced to the initiation reaction $O_2 + H_2O \rightarrow OH^{\cdot} + HO_2^{\cdot}$, which requires relatively low activation energy. In the outside liquid region, the dispersion of radicals is limited by robust recombination reactions. The simulated penetration depth of $OH^{\cdot}$ is around 0.2 μm and agrees with reported experimental measurements. The proposed numerical approach can be employed to better capture the radical activity and is instrumental in optimizing the engineering application of sonochemistry.

1. Introduction

Sonochemistry has been recognized as a promising advanced oxidation process with the capability of degrading various contaminants effectively, including phenol [1], hydrocarbons [2], pesticides [3], and polymers [4]. The versatility of sonochemistry is rooted in acoustic cavitation: the formation, growth, and violent collapse of microbubbles in sonicated liquids [5]. In the last stage of the dynamic phase, compressional heating creates hotspots inside the bubble, with temperatures as high as that on the surface of the sun [6]. For volatile pollutants such as carbon tetrachloride, their pyrolysis in the interior of the collapsing bubble is the main degradation pathway [7–9]. For nonvolatile species, however, the reactive species produced and diffused out from the cavitation bubble are primarily responsible.

For the bubbles undergoing stable oscillation, the oxidation potential of cavitation-induced radicals depends on two integral steps: the production of the radicals inside the collapsing bubble, and their dispersion in the bulk solutions. The radicals generated in the first step determine the categories and amounts of the oxidants, while the distribution in the second step influences the probability of the interaction with the pollutants. A schematic showing the complete process is displayed in Fig. 1. Another route for the radicals to get into contact with the contaminants is the breakup of the bubble. In this situation, the radicals are released into the solution directly. As many unknowns exist for this case (e.g. the time of the breakup, the disturbed flow field surrounding the bubble, etc.), we don't consider the latter process in the present study.

Owing to the transient nature of the oscillating bubble, numerical simulation has been traditionally used to investigate the radicals in acoustic cavitation [10–13]. Desirably, the numerical models should account for both the production and dispersion integratedly, since they form a complete process for the radicals to realize the oxidation potential. However, previous studies [10–13] have exclusively focused on the radical production inside the bubble, while the dispersion process in the aqueous medium is generally ignored. In consequence, a full picture of the radical behavior around the transient bubble is still missing.

Even for the most examined production part, considerable opacities remain regarding the exact chemical activities in the collapsing bubble. In most cases, the chemical simulations from past literature only reported the produced quantity of the various radicals. Vital information

---

Nomenclature

a, b	van der Waals constants, J·m^3/mol^2, m^3/mol
B	constant for the equation of state for water, $B = 321$ MPa
c	species concentration, mol/m^3
c_p, c_v	heat capacity at constant pressure (volume), J/(K ·mol)
C	speed of sound in water at the bubble wall, m/s
D	Mass diffusivity in water, m^2/s
f	Acoustic frequency, Hz
ΔE	reaction energy, kJ/mol
H	enthalpy of water at the bubble wall, J/kg
k	rate coefficient, m^3/(mol·s)
k_B	Boltzmann constant, $k_B = 1.38 \times 10^{-23}$ J/K
L	latent heat of vaporization, J/mol
M	molecular weight, g/mol
n	amount of species, mol
N	number of species particles, []
p	pressure, Pa
R	bubble radius, μm
S	bubble surface, m^2
r	radial coordinate
T	temperature, K
t	time, s
Q	heat flux, J
V	bubble volume, m^3

Greek Symbols

ε	constant in the equation of state for water, $\varepsilon = 7$
μ	viscosity of water, Pa·s
δ	thickness of the boundary layer, m
Θ	uptake coefficient, $\Theta = 0.001$
Γ	flux of radicals at the bubble interface, mol/s
$\mathscr{R}$	universal gas constant, $R = 8.31$ J/(K·mol)
κ	thermal conductivity, W/(m·K)
ρ	density, kg/ m^3
υ	molar volume, m^3/mol

subscripts

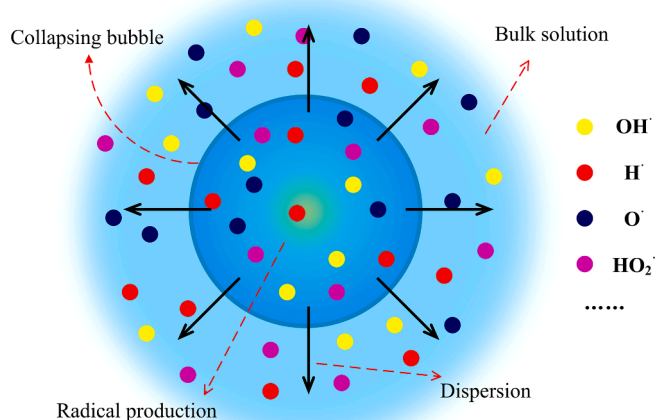|	
aq	aqueous
sat	saturation
a	acoustic
l	liquid
g	gas
i	species index
w	bubble wall
v	vapor
mix	gas mixture
b	bubble
∞	reference state at infinite
γ	reaction index

Fig. 1. schematic showing the radical production and dispersion around a collapsing bubble.

in terms of the exact reactions responsible for the generation of a specific radical is not accessible. However, such information may be crucial in interpreting some sonochemical phenomena. For example, prior tests showed that dissolving oxygen in water is more efficient than using argon in inducing hydroxyl radicals [14–16]. This is counterintuitive at first glance since a much lower collapsing temperature is formed in the oxygen bubble [14,17,18]. Lacking sufficient knowledge of the reaction details, some researchers guessed that the enhanced radical production is caused by the additional dissociation of oxygen molecules via $O_2 \rightarrow 2O^\bullet$ and $O^\bullet + H_2O \rightarrow 2OH^\bullet$ [14,17,19]. This conjecture is not convincing when taking into account that the dissociation energy of oxygen is as high as that of water molecules (493.4 kJ/mol versus 492.2 kJ/mol) [20,21]. With decreased collapsing temperature, the overall yields of hydroxyl radicals should still be lowered. We argue that issues as such

can only be solved by a complete understanding of the reaction kinetics in the radical productions.

In this paper, an integrated numerical scheme is proposed to close the abovementioned knowledge gaps. The main components for this scheme are introduced in Section. 2 with two subsections, each detailing the radical production and the dispersion in the liquid region. In Section.3, we use two typical cases to demonstrate the applicability of the proposed scheme: one for an argon bubble and another for an oxygen bubble. Also in this section, we propose a new theory to explain how the existence of oxygen in the bubble increases the production of hydroxyl radicals. Section. 4 discusses some unresolved issues around the interfacial chemistry that may affect the reported simulation results. Several implications derived from this study are also highlighted in the context of sonochemical degradation of chemical compounds. Finally, the main findings are concluded in Section. 5.

2. Formulation

We consider a spherical bubble oscillating in water under ultrasonic driving. The water is saturated with either argon or oxygen. At the initial state, the bubble is assumed to contain water vapor and the saturated gas. As the bubble expands in the rarefaction phase of ultrasound, additional water molecules would enter the interior through evaporation at the gas–liquid interface. At the collapse stage, chemical reactions among the gases generate various radicals. Parts of the produced radicals would penetrate the gas–liquid interface and diffuse into the surrounding liquid. In the following sections, the models for radical production and dispersion are introduced separately.

2.1. The model for radical production

The free radicals are produced through chemical reactions in the collapsing bubble and are intrinsically associated with the bubble dynamics. The radial oscillation of the bubble determines the intracavity conditions, i.e., the temperature and pressure, for the reactions, while the latter would in turn affect the temperature via releasing/absorbing reaction energy and change the bubble composition through creating/

destructing chemical species. In our method, the bubble dynamics are simulated with the Gilmore model [22]. The heat and mass transfer between the bubble and the ambient liquid are also accounted for. For the simulation of chemical reactions, two mechanisms are used: the comprehensive GRI-Mech 3.0 [23] for the argon bubble, and the state-of-the-art $H_2/O_2/H_2O$ mechanism [24] for the oxygen bubble. The coupled simulation yields the category and quantity of radicals at each moment in the bubble collapse. The implementation details of these models are presented in our recent publication [25] and therefore will not be elaborated here. We only listed the corresponding equations in Table.1 with the parameters explained in the Nomenclature. In the following, we stress several key points regarding the application of these models.

Firstly, both the temperature and pressure are treated as homogenous inside the bubble. Since thermal conduction at the interface is the main energy dissipation mechanism for the bubble [26,27], the heat transfer between the bubble and the ambient liquid is calculated based on the temperature gradient through assumed thermal boundary layers. Stricker *et al.* [28] demonstrated that the estimated temperatures using this method are close to the results from solving the full energy equations and can be reliably applied in sonochemistry simulation. The technique in our method involves two thermal boundary layers, one in the gas phase and another in the surrounding liquid. The heat transfer is estimated as thermal conduction through these layers.

Secondly, the GRI-Mech 3.0 mechanism used for the chemical simulation in argon bubble contains all the radical species of interest in sonochemistry study, including OH$^\bullet$, H$^\bullet$, O$^\bullet$, HO$_2^\bullet$, and H_2O_2. It has been optimized through a systematic procedure and extensively validated [29]. Its reliability in simulating cavitation-related chemistry has also been verified before [25] using test data from Kalus *et al.* [30,31]. Owing to the huge number of reactions involved in this mechanism, the complete reaction data is not listed here but can be accessed from the database [23]. The $H_2/O_2/H_2O$ reaction mechanism [24] for the oxygen bubble contains the species O_3 and HO$_3^\bullet$ in addition to the radicals mentioned above. The rate parameters of the reactions are updated continuously and represent the latest development for the simulation of high-temperature gas reactions. As in the case of GRI-Mech 3.0, the reaction data is not listed here for brevity. The readers are referred to the literature [24] for a complete description of this mechanism.

Thirdly, all the chemical simulations are conducted on the open-source platform Cantera [32]. The most significant advantage conferred by using Cantera is that it allows real-time analysis of the reaction pathways. By tracing the flow of a specific element, the reactions responsible for the production of certain radicals can be accurately identified. This is a critical improvement compared with previous simulations. The associated benefits will be illustrated in the production mechanism analysis in Section 3.

2.2. The model for radical dispersion

The radical dispersion includes two simultaneous processes: the mass diffusion driven by the concentration gradient, and the chemical reactions among the radicals as well as with the saturated gas. The diffusion–reaction equation governing the dispersion can be expressed as:

$$\frac{\partial c_i}{\partial t} + \dot{R}\left(\frac{R}{r}\right)^2\frac{\partial c_i}{\partial r} = \frac{D_i}{r^2}\frac{\partial}{\partial r}\left(r^2\frac{\partial c_i}{\partial r}\right) + \sum_j \alpha_{i,j}\gamma_j \qquad r > R \qquad (1)$$

where r is the radial coordinate with $r = 0$ denoting the bubble center and $r = R$ the bubble wall, $c_i(r, t)$ the molar concentration of the species i at time t and distance r in the liquid, D_i the diffusion coefficients, $R(t)$ the instant bubble radius, and $\dot{R}(t)$ the velocity of the bubble wall. Both $R(t)$ and $\dot{R}(t)$ come from the bubble dynamics simulation. The values of D_i for the species discussed in this study are listed in Table.2.

The last term in Eq 1 represents the rate of concentration change due to chemical reactions, in which $\alpha_{i,j}$ is the stoichiometric weight of species i in the reaction γ_j. The main radicals produced from the investigated bubbles are OH$^\bullet$, H$^\bullet$, O$^\bullet$, HO$_2^\bullet$, as well as O_3 and HO$_3^\bullet$ for the oxygen bubble. When they dissolve in the bulk liquid, the possible chemical reactions and the associated rate constants are listed in Table.3. They are taken from previous studies of plasma-liquid interaction and have been widely adopted for simulating the radical reactions in aqueous solutions [33,34]. Categorially, they can be divided into radical recombination, and the attack of radicals on the recombination products, dissolved molecular gases, and water molecules. Additional reactions with other chemical compounds may occur in the wastewater environment. In this study, the sonicated water is assumed as *neat* and those reactions are not considered.

The radicals are supplied from the bubble with the time-varying flux Γ_i. At infinite, their concentrations are assumed to reach the asymptotic value. The corresponding boundary conditions for Eq 1 thus become.

$$\begin{aligned} 4\pi R^2 D_i\partial_r c_i &= \Gamma_i & r = R \\ \partial_r c_i &= 0 & r\rightarrow\infty \end{aligned} \qquad (2)$$

Determining the value of Γ_i is the trickiest part of this simulation. Large uncertainty exists when the radicals are transported through the gas–liquid interface. Since there is no reported experimental measurement, we refer to two proposed approximations to estimate Γ_i. The first uses an uptake coefficient defined as [35,36]:

Table 2
The diffusion coefficients of the species in water, 10^{-5} cm^2/s.

OH$^\bullet$	H$_2$O$_2$	O	H$^\bullet$	HO$_2^\bullet$	H$_2$	O$_2$	O$_3$	HO$_3^\bullet$
2.3	1.0	2.0	4.5	1.0	4.5	1.97	1.7	1.0

Table 1
The model for simulating the bubble dynamics and intracavity chemical reactions. The specifications for the parameters are listed in the Nomenclature table.

components	equations	Key parameters or implementation
Bubble radial dynamics	$\left(1 - \frac{\dot{R}}{C}\right)R\ddot{R} + \frac{3}{2}\left(1 - \frac{\dot{R}}{3C}\right)\dot{R}^2 = \left(1 + \frac{\dot{R}}{C}\right)H + \left(1 - \frac{\dot{R}}{C}\right)\frac{R}{C}\dot{H}$	$H = \frac{\varepsilon}{\varepsilon - 1}\frac{(p_\infty + B)^{\frac{1}{\varepsilon}}}{\rho_\infty} \times \left[(p_b + B)^{\frac{\varepsilon - 1}{\varepsilon}} - (p_\infty - p_a\sin(2\pi ft) + B)^{\frac{\varepsilon - 1}{\varepsilon}}\right]$ $p_b = p_g - \frac{2\sigma}{R} - \frac{4\mu\dot{R}}{R}, P_g = \frac{\mathscr{R}T_b}{v - b} - \frac{a}{v^2}$
Energy balance	$\dot{E} = -p_g\dot{V} + \dot{Q} + \dot{n}_{H_2O}c_v T_w + \dot{E}_{chem}$	
Heat transfer	$\dot{Q}\vert_g = 4\pi R^2\kappa_{mix}(T_w - T_b)/\delta_g \dot{Q}\vert_l = 4\pi R^2\kappa_l\frac{\partial T}{\partial r}\Big\vert_{r=R} - \dot{n}_{H_2O}L$	$\delta_g = \min\left[\left(\kappa_{mix}/(\rho_{mix}c_{p,mix})R\sqrt{\rho_l/p_b}\right)^{0.5}, R/\pi\right]$ $\delta_l = \min\left[\left(\frac{\kappa_l}{\rho_l c_{p,l}}\frac{R}{\sqrt{p_b/\rho_l}}\right)^{0.5}, \frac{4\pi R^2 k_l}{L\vert\dot{n}_{H_2O}\vert}\right]$
Mass transfer	$\dot{n}_{H_2O} = 4\pi R^2\frac{\alpha_M(p_{sat} - p_v)}{\sqrt{2\pi M_{H_2O}\mathscr{R}T_w}}$	$p_v = p_g n_{H_2O}/n_{total}$, $p_{sat}\propto T_w$
Chemical reactions	GRI-Mech 3.0; $H_2/O_2/H_2O$ reaction mechanism	Conducted on the platform Cantera.

Table 3
The chemical reactions with the rate coefficients in the liquid [33,34].

No.	Reactions	Rate coefficients ($M^{-1}s^{-1}$, $1\ M = 1 \times 10^3$ mol/m^3)
R.1	$OH^{\bullet}_{(aq)} + OH^{\bullet}_{(aq)} \rightarrow H_2O_{2(aq)}$	3.6×10^9
R.2	$O^{\bullet}_{(aq)} + O^{\bullet}_{(aq)} \rightarrow O_{2(aq)}$	2.8×10^{10}
R.3	$H^{\bullet}_{(aq)} + H^{\bullet}_{(aq)} \rightarrow H_{2(aq)}$	7.8×10^9
R.4	$H^{\bullet}_{(aq)} + OH^{\bullet}_{(aq)} \rightarrow H_2O_{(aq)}$	7.0×10^9
R.5	$H^{\bullet}_{(aq)} + H_2O_{2(aq)} \rightarrow OH^{\bullet}_{(aq)} + H_2O_{(aq)}$	9.0×10^7
R.6	$H^{\bullet}_{(aq)} + O_{2(aq)} \rightarrow HO_{2\ (aq)}$	2.1×10^{10}
R.7	$H^{\bullet}_{(aq)} + HO^{\bullet}_{2\ (aq)} \rightarrow H_2O_{2(aq)}$	1.8×10^{10}
R.8	$OH^{\bullet}_{(aq)} + HO^{\bullet}_{2\ (aq)} \rightarrow H_2O_{(aq)} + O_{2(aq)}$	6.0×10^9
R.9	$OH^{\bullet}_{(aq)} + H_{2(aq)} \rightarrow H_2O_{(aq)} + H^{\bullet}_{(aq)}$	4.3×10^7
R.10	$H_2O_{2(aq)} + OH^{\bullet}_{(aq)} \rightarrow HO^{\bullet}_{2\ (aq)} + H_2O_{(aq)}$	2.7×10^7
R.11	$HO^{\bullet}_{2\ (aq)} + HO^{\bullet}_{2\ (aq)} \rightarrow H_2O_{2(aq)} + O_{2(aq)}$	7.0×10^5
R.12	$H_2O_{2(aq)} + O^{\bullet}_{(aq)} \rightarrow HO^{\bullet}_{2\ (aq)} + OH_{(aq)}$	1.6×10^5
R.13	$O^{\bullet}_{(aq)} + H_2O_{(aq)} \rightarrow OH_{(aq)} + OH^{\bullet}_{(aq)}$	1.3×10^4
R.14	$H^{\bullet}_{(aq)} + H_2O_{(aq)} \rightarrow H_{2(aq)} + OH^{\bullet}_{(aq)}$	1.0×10^1
R.15	$H_{2(aq)} + H_2O_{2(aq)} \rightarrow H^{\bullet}_{(aq)} + OH^{\bullet}_{(aq)} + H_2O_{(aq)}$	6.0×10^6
R.16	$O_{2(aq)} + O^{\bullet}_{(aq)} \rightarrow O_{3(aq)}$	4.0×10^9
R.17	$H_{(aq)} + O_{3(aq)} \rightarrow HO^{\bullet}_{3\ (aq)}$	3.8×10^{10}
R.18	$OH_{(aq)} + O_{3(aq)} \rightarrow HO^{\bullet}_{2\ (aq)} + O_{2(aq)}$	1.1×10^8
R.19	$HO^{\bullet}_{2\ (aq)} + O_{3(aq)} \rightarrow HO_{3(aq)} + O_{2(aq)}$	5.0×10^8
R.20	$HO^{\bullet}_{3\ (aq)} \rightarrow OH^{\bullet}_{(aq)} + O_{2(aq)}$	1.1×10^5
R.21	$H_2O_{2(aq)} + O_{3(aq)} \rightarrow OH^{\bullet}_{(aq)} + HO^{\bullet}_{2\ (aq)} + O_{2\ (aq)}$	3.0×10^9

$$\Theta = \frac{N_{in} - N_{out}}{N_{coll}} \tag{3}$$

which characterizes the fraction of molecules that penetrate the liquid through the bubble interface. N_{in} represents the number of molecules evading the liquid, N_{out} is the number of molecules that reflect from the liquid, and N_{coll} the total molecules that collide with the gas–liquid interface. With this coefficient, the flux can be calculated according to the molecular dynamics theory [10].

$$\Gamma_i = 4\pi R^2 \Theta c_{i,b} \sqrt{\frac{k_B T_b}{2\pi M_i}} \tag{4}$$

In which $c_{i,b}$ is the particle density of the species inside the bubble, T_b the bubble temperature, k_B the Boltzmann constant, and M_i the molecular weight of the species. By setting $\Theta = 0.001$, Yasui *et al.* [10] found that the simulated number of OH radicals dissolved from a SBSL bubble into liquid water matches well with the experimental data [37]. We adopt this value in the simulation.

Another method assumes that the dissolution of radicals occurs in the manner of diffusion through a boundary layer. Then the flux can be estimated by the concentration gradient [11,12,38]:

$$\Gamma_i = 4\pi R^2 D_{i\text{-}g} \frac{c_{i,b} - c_{i,0}}{l_i}$$

$$\text{with} \quad l_i = \min\left(\sqrt{\frac{RD_{i\text{-}g}}{|\dot{R}|}}, \frac{R}{\pi}\right) \tag{5}$$

where $c_{i,0}$ is the species concentration at the bubble wall, and $D_{i\text{-}g}$ the mass diffusion constant among the gas mixture in the bubble. Since most radicals are highly soluble in water, $c_{i,0}$ is assumed as zero.

In the Discussion section, it is shown that while quantitative differences between these two methods can be observed in the dissolution of radicals at the bubble, the influence on the dispersion process is not significant. In the following case studies, the uptake method is employed unless otherwise specified.

2.3. Numerical method

The methods for simulating the bubble dynamics and the chemical

reactions have been introduced in our previous studies [25,39–41]. Therefore, only the method for the dispersion simulation is illustrated in this section. To solve the diffusion–reaction equation (Eq 1), we split the reaction term from the equation and calculate the diffusion and reaction process sequentially at each time step. The rationale for this treatment lies in the vastly disparate time scales for mass diffusion and chemical reactions. For the typical case considered in the present simulation, the time scale for bubble oscillation around the collapse point $t_{osc} = R/|dR/dt|$ is about 10^{-9} s. When the characteristic length is set with the equilibrium bubble radius $R_0 = 10$ μm, the time scale of mass diffusion for OH$^{\bullet}$ radicals can be estimated as $t_d = R_0^2/D_{OH}$ and is in the order of 10^{-1} s, while that for recombination reaction is about 10^{-7} s. Based on this distinction, it is expected that the dispersion process is characterized by rapid chemical reactions followed by slow diffusions. Therefore, a separate calculation of reaction and diffusion at each time step is justified.

The now pure diffusion equation is solved by the numerical method proposed by Hegedűs *et al.* [42]. They introduced a new variable ζ to transform the Eulerian coordinates into the Lagrangian ones and convert the unbounded liquid domain into the bounded one [42]:

$$\zeta = \frac{R}{r} \qquad \zeta \in [0, \ 1] \tag{6}$$

Then the diffusion equation becomes:

$$\frac{\partial c_i}{\partial t} - \frac{\dot{R}}{R}(\zeta^4 - \zeta)\frac{\partial c_i}{\partial \zeta} = D_i \frac{\zeta^4}{R^2}\frac{\partial^2 c_i}{\partial \zeta^2} \tag{7}$$

with c_i now being a function of ζ and t. Discretizing the spatial domain $\zeta \in [0,1]$ into the Gauss-Lobatto points.

$$\zeta_k = \cos\left(\frac{\pi}{2}\frac{m - k}{m - 1}\right), \quad k = 1, ..., m \tag{8}$$

and approximating the derivative terms with the central difference method, the diffusion equation is written as a set of algebraic equations and can be solved readily. In our calculation, we used 100 points for the Gauss-Lobatto discretization and further refined the grids near the interface by adding 16 points in the first 5 layers to ensure sufficient spatial resolution. Other methods like the Galerkin or spectral collocation approach can be also used to solve the diffusion equation. A comparison of the efficiency between the different methods is reported by Hegedűs *et al.*[42].

For the time marching, we employed the fully implicit method coupled with an adaptive time step scheme to maintain numerical stability. The absolute error in the calculated radical concentration between two consecutive steps is controlled to be lower than 0.001 mol/m^3. After the diffusion calculation is completed, the chemical simulation based on the reactions in Table. 3 is conducted and the concentration field is updated.

The initial bubble composition is determined by applying equilibrium condition [7,8,39]:

$$n_{H_2O,0} = \frac{p_{v,sat}V}{\mathscr{R}T_\infty}, \qquad n_{g,0} = \frac{(p_0 - p_{v,sat})V}{\mathscr{R}T_\infty} \tag{9}$$

where $n_{H_2O,0}$ and $n_{g,0}$ are the initial amounts of water vapor and gas (argon or oxygen), $p_{v,sat}$ the saturated vapor pressure, V the bubble volume, $\mathscr{R}$ the gas constant, T_∞ the ambient pressure and temperature, and p_0 the total bubble pressure. From the pressure balance for the bubble, p_0 is calculated by.

$$p_0 = p_\infty + \frac{2\sigma}{R_0} \tag{10}$$

in which p_∞ is the ambient pressure, σ the surface tension, and R_0 the initial radius of the bubble. The initial concentration of radicals is assumed to be zero and those of dissolved gases are taken as the

saturated values.

3. Case study

In this section, the proposed numerical scheme is applied to two typical cases where argon or oxygen is saturated in water. A similar experiment has been conducted to examine the sonochemical production of free radicals [14]. Corresponding to the referenced test, the bubble is assumed to oscillate under the acoustic driving with the amplitude $p_a = 1.3$ bar and frequency $f = 20$ kHz. The equilibrium radius $R_0 = 10$ μm and the temperature of ambient water $T_\infty = 298$ K. It should be noted that besides the saturated gas, the bubble also contains water vapor and various species created by chemical reactions. However, for brevity and comparison, we will still refer to the bubble in each case as argon or oxygen bubble without further explicitly indicating the presence of other species.

3.1. The argon bubble

3.1.1. Bubble dynamics and radical productions

Fig. 2(a) and (b) show the bubble dynamics and the productions of the main reactive species inside the argon bubble within the first 6.5 acoustic cycles. Under the prescribed acoustic driving, the periodic oscillation of the bubble is quite stable and shows a strong nonlinearity, indicating the violent motion in the compression stage. The peak temperature in the bubble collapse reaches 5619 K, suggesting the extreme intracavity condition. As a monatomic gas, argon has a relatively large polytropic index and small thermal conductivity. The former property points to a lower heat capacity that is preferential for compressional heating, while the latter dictates that the thermal loss to the ambient liquid is small when the bubble is heated. The chemical reactions in the collapse produce hydroxyl radical (OH·), hydrogen atom (H·), oxygen atom (O·), hydrogen peroxide (H_2O_2), and hydroperoxyl radical (HO·$_2$), in descending order by the produced amount in one acoustical cycle.

Table. 4 summarizes several parameters that quantify the production of the main radicals, including the peak number of the radical particles, $N_{i\text{-max}}$, the maximum concentration, $c_{i\text{-max}}$, inside the bubble, and the accumulative number of molecules dissolved in the liquid in one acoustic cycle, $\Delta N_{i\text{-}s}$. The data shows that despite the small number of

Table 4
The productions of the main reactive species in the argon bubble: $c_{i\text{-max}}$ is the maximum density of the molecules in mol/m^3, $N_{i\text{-max}}$ the peak number of particles inside the bubble, and $\Delta N_{i\text{-}s}$ the accumulative number of the species dissolved in the liquid in one acoustical cycle.

Species	OH·	H·	O·	HO·$_2$	H_2O_2
$N_{i\text{-max}}$	6.1×10^9	8.4×10^8	7.1×10^8	1.2×10^7	8.6×10^6
$c_{i\text{-max}}$	631.5	78.1	50.2	0.4	0.3
$\Delta N_{i\text{-}s}$	3.5×10^9	1.1×10^9	5.9×10^8	5.2×10^6	4.6×10^6

radicals produced in a single collapse, their particle density can be enormous inside the strongly compressed bubble. Especially, the value of $c_{i\text{-max}}$ for OH· is as high as 631.5 mol/m^3, implying huge oxidation potential at the collapse point if the bubble disintegrates at this moment. Very large values of $c_{i\text{-max}}$ are also observed for O· and H· atoms. Similar results have been reported in the case of laser-induced bubbles [25].

3.1.2. Reaction pathway analysis

The productions of radicals last for dozens of nanoseconds in the collapse as shown in Fig. 3(a), where the number of radicals is displayed as the collapse progresses around the collapse point. In the figure, a new time parameter t^* is adopted with $t^*=0$ denoting the moment when $R = R_{\min}$. It is observed that the radicals are produced sequentially with the OH· and H· emerging first. The reaction pathways of H atoms at $t^*=-3.8$ ns displayed in Fig. 3(b) suggest that the thermal dissociation of water molecules is responsible for the generation of OH· radicals and H· atoms at this early stage:

$$H_2O + M \rightarrow H\cdot + OH\cdot + M \tag{R22}$$

Note that this reaction is also the initiation step for whole chemical reactions in the argon bubble. With the activation temperature as high as 59700 K for this reaction, a very high energy barrier must be overcome before other radicals can be generated.

After the reactions are activated, the H· atoms produced from the reaction R22 would attack water molecules and create additional OH· radicals as shown in Fig. 3(b):

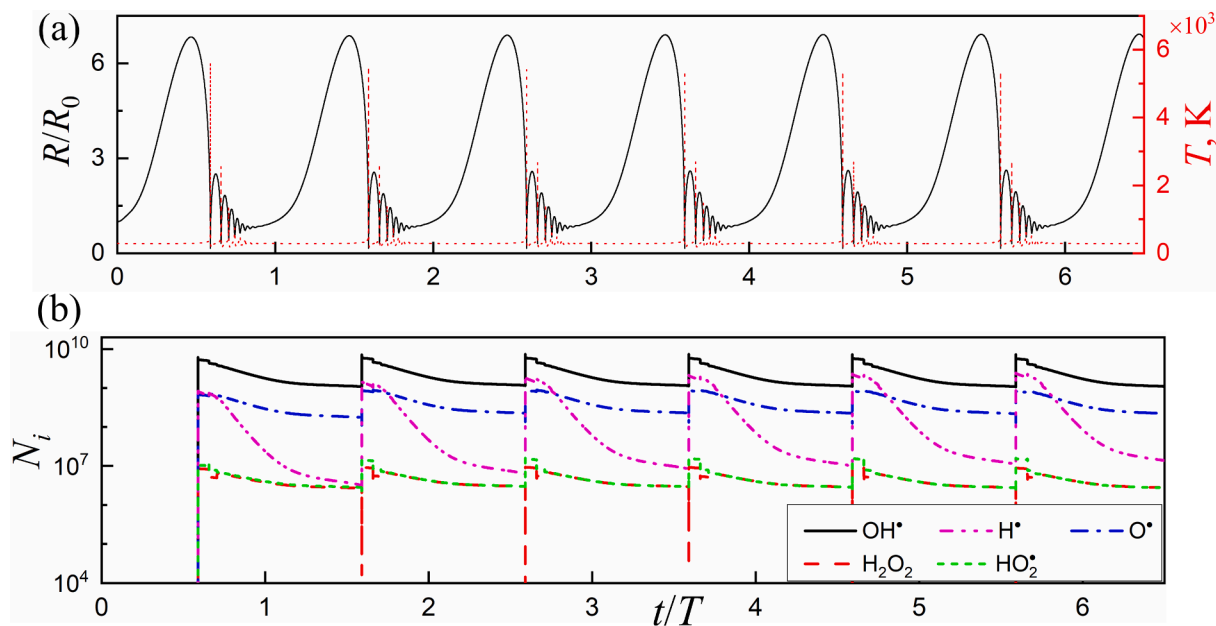$$H_2O + H\cdot \rightarrow H_2 + OH\cdot \tag{R23}$$

Fig. 2. The bubble dynamics and productions of free radicals inside the argon bubble within the period of 6.5 acoustic cycles: (a) The evolution of bubble radius; (b) The temporal variation of the number of particles for the main radical products. The parameters for the calculated case are: $p_a = 1.3$ bar, $f = 20$ kHz, $R_0 = 10$ μm, and $T_\infty = 298$ K.
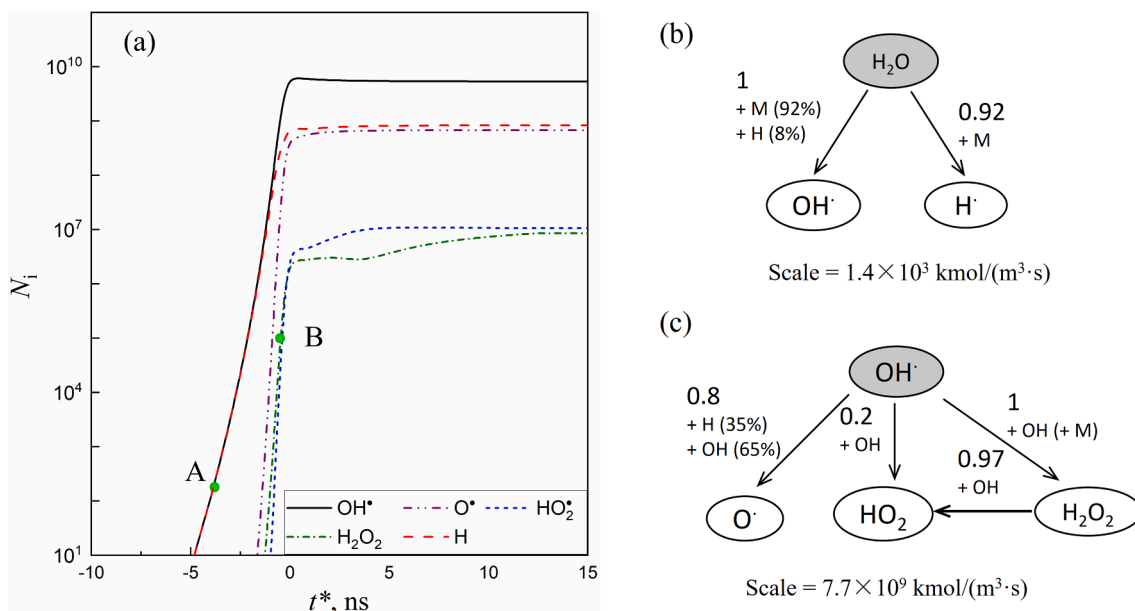
Fig. 3. (a) the productions of radicals around the collapse point in the argon bubble where $t^*=0$ corresponds to the collapse point when $R = R_{min}$; (b)The reaction pathways of H atoms at $t^*=-3.8$ ns. The reaction condition in the bubble at this moment is $T_b = 2442$ K and $p_g = 26$ MPa; (c) The reaction pathways of O atoms in the argon bubble at $t^*=-0.5$ ns. The reaction condition in the bubble at this moment is $T_b = 5584$ K and $p_g = 1349$ MPa. These two moments are represented by "A" and "B" in figure (a). All the reactions involved in a certain pathway are indicated above the arrow and the contribution of each reaction is labeled. The numbers in the pathway denote the flux of H or O atoms with the scale given at the bottom of the figure. M denotes the third body in the reactions.

As more OH' and H' are produced and the temperature inside the bubble continues to increase, the reactions become increasingly complicated. Fig. 3(c) displays that at $t^*=-0.5$ ns, O' atoms are produced by the following reactions.

$$OH^. + OH^. \rightarrow H_2O + O^. \qquad (R24)$$

$$OH^. + H^. \rightarrow H_2 + O^. \qquad (R25)$$

These two reactions are barrierless and can proceed rapidly once the supply of the reactants (OH' and H') is adequate.

For H_2O_2 and HO'$_2$, their productions rely on the recombination of OH' radicals:

$$OH^. + OH^. + M \rightarrow H_2O_2 + M \qquad (R26)$$

$$OH^. + OH^. \rightarrow H^. + HO_2^. \qquad (R27)$$

Similar to R24 and R25, the above two reactions are also barrierless. For HO'$_2$, there is another production channel where OH' reacts with H_2O_2:

$$OH^. + H_2O_2 \rightarrow HO_2^. + H_2O \qquad (R28)$$
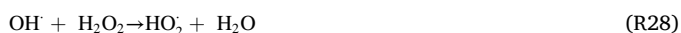
The preceding analysis reveals that the reactions in the argon bubble progress in a cascading way. It is provoked by the initiation reaction (dissociation of water molecules, R22) and proceeds with the products from the previous reactions acting as the reactants for the next reactions. The high energy barrier of the initiation reaction is the major factor limiting the radical productions.

3.1.3. Radical dispersion

Before analyzing the dispersion of the radicals in the liquid phase, we first examine the dissolution behavior at the bubble interface. Fig. 4 displays the concentration of the radicals and their recombination products at the gas–liquid interface ($r = R$). Note again that the new time parameter t^* is used in order to illustrate the nuanced dynamics near the collapse point. It is seen that the time duration of the radicals at the interface is rather short. Owing to the small diffusivity, the main radicals OH', H', and O' attain peak concentration in several nanoseconds.
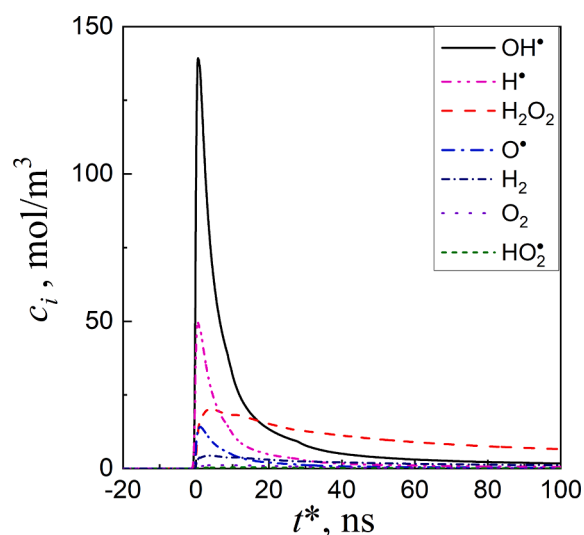

Fig. 4. The dissolution of radicals at the gas–liquid interface ($r = R$) for the argon bubble. The concentration of main radicals and recombination products are shown around the collapse ($R = R_{min}$).

Afterward, the strong recombination reactions quickly consume the main body of radicals, leaving only a small part to diffuse away.

The complete dispersion process within the first 6.5 acoustic cycles is displayed in Fig. 5 for the main radicals OH', H', and O'. As a result of the slow diffusion and rapid recombination reaction, a concentration profile with a sharp gradient is observed in the near liquid region. The penetration depth of OH' radicals is about 0.2 μm, which agrees well with experimental results from previous investigations [43,44]. For H' and O', this distance is shorter due to fewer supplies from the interior of the bubble and the higher rate of recombination reaction (see Table.3). As the bubble collapses periodically, the release and dispersion of radicals are also intermittent.

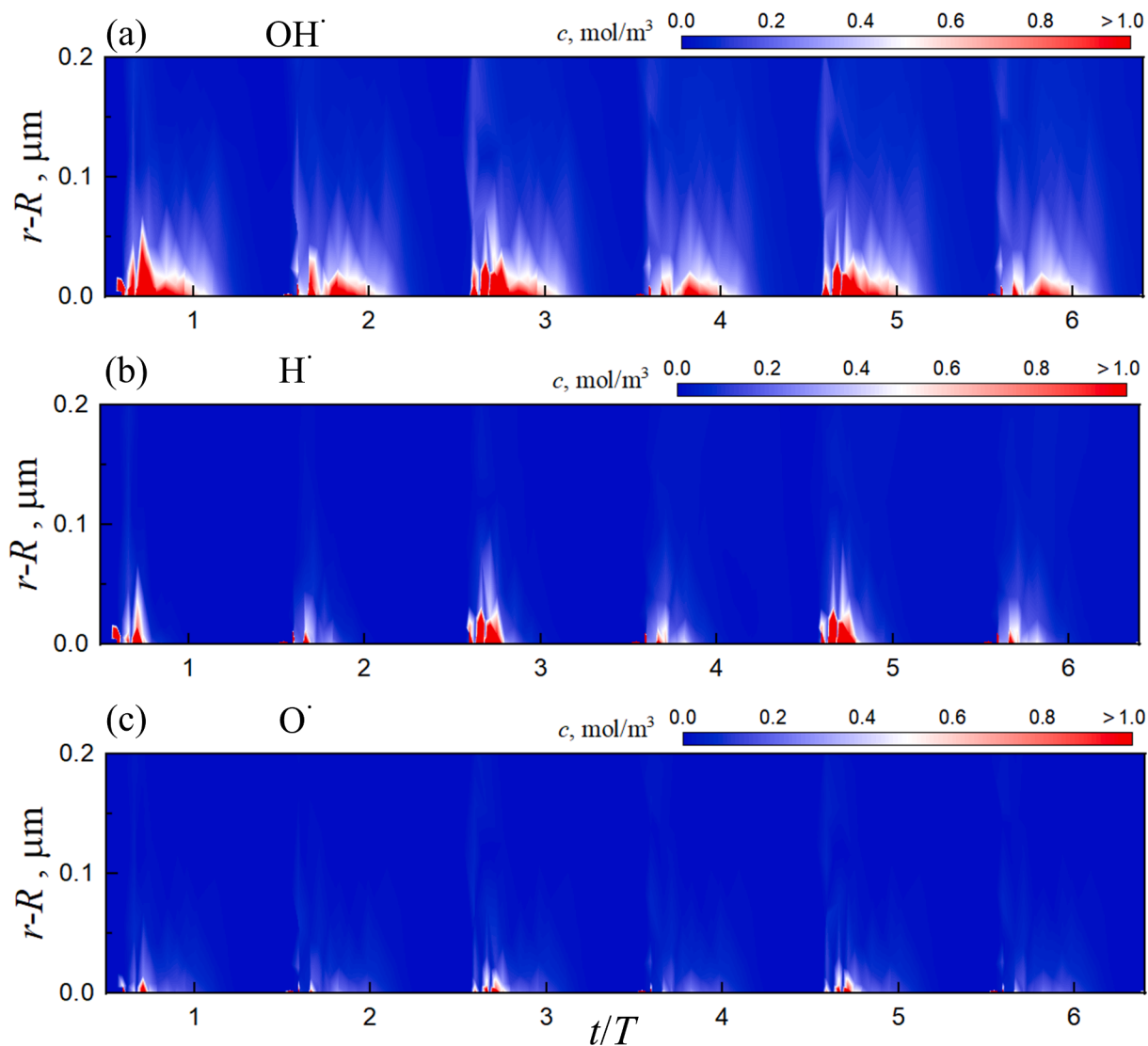The dispersion pattern of the recombination products H_2O_2 and H_2 is

Fig. 5. The dispersion of different radicals in the liquid for the argon bubble: (a) OH˙ radicals; (b) H˙ atoms, and (c) O˙ atoms. The ordinate shows the radial position in the ambient liquid and the abscissa denotes the time t normalized by the acoustical cycle T, $T = 1/f$. The maximum concentration for each radical species is not indicated in the figure but can be referenced from Fig. 4. Since the high concentration lasts briefly, in order to present a better image of the radical dispersion, all the regions with concentrations larger than 1 mol/m³ are colored red.
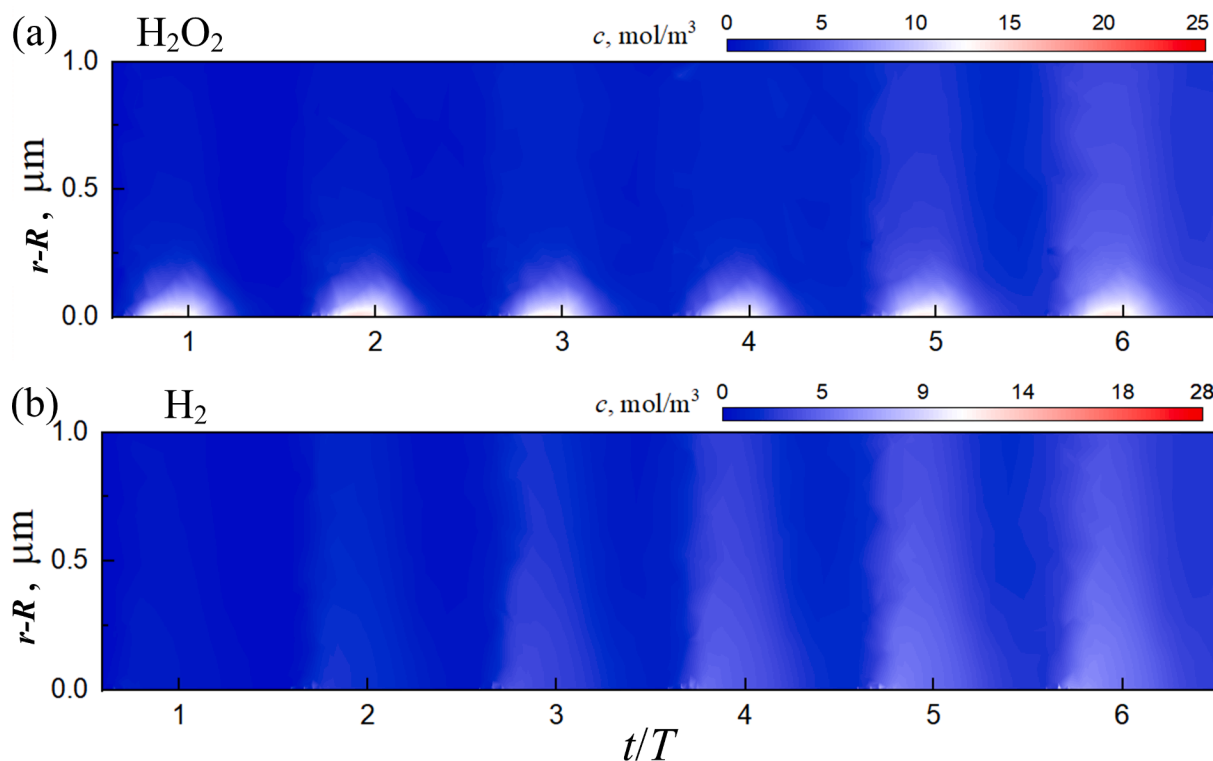
Fig. 6. The dispersion of recombination products in the liquid for the argon bubble : (a) H_2O_2; (b) H_2.

different from that for the radicals as shown in Fig. 6. We stress that the diffusion of these stable species is very slow due to the small diffusivity in water. Modeling such long-term behavior involves a huge number of bubble oscillations and is out of the scope of this paper. Still, the results presented in Fig. 6 offer a glimpse of the dispersion pattern for these products.

After being produced at the bubble interface, H_2O_2 and H_2 gradually diffuse away in the liquid. The periodicity in the generation and propagation is obvious in Fig. 6. With each bubble collapse, new H_2O_2 and H_2 molecules are created at the interface. The periodic supply sustains the consistent diffusion with increasing concentration in the near liquid region. At the end of 6.5 cycles, the traveling distance of H_2O_2 and H_2 is about 1 μm. It should be noted that the investigated case assumes that only the inert argon is dissolved in the water. When other reactive species exist in the solution, a part of recombination products, especially the H_2O_2, will be consumed and the diffusion distance will be shortened.

3.2. The oxygen bubble

3.2.1. Bubble dynamics and radical productions

In this section, we turn our attention to the case where oxygen is saturated in the water. Fig. 7(a) shows that while the pattern of bubble dynamics is similar to that for the argon bubble, much milder conditions are generated inside the oxygen bubble when it collapses. The maximum temperature is only 3692 K compared with the 5619 K attained in the argon bubble. This difference is expected considering the physical properties of oxygen, i.e., the relatively small polytropic index and large thermal conductivity. Fig. 7(b) indicates that the most produced reactive species is still OH•, but a large quantity of O•, $HO_2^•$, and O_3 is also created.

As with the case of the argon bubble, the parameters quantifying the

production of radicals in the oxygen bubble are also obtained and presented in Table.5. Comparing the data in Table.4 and 5 reveals that while fewer H• are produced in the oxygen bubble than in the argon bubble, more OH•, O•, $HO_2^•$, and H_2O_2 are generated in the former case. Measured by the total quantity of reactive species, the oxygen bubble yields a higher output of radicals than the argon bubble, which matches conclusions from previous reports [14–16].

3.2.2. Reaction pathway analysis

To account for the diverging trends in the collapsing temperature and radical production in the oxygen bubble, the reaction kinetics are investigated by the analysis of reaction pathways shown in Fig. 8.

As the bulk of produced radicals is oxidants for the oxygen bubble, we only present the reaction pathways of O atoms at t^*=-5 ns and -0.4 ns, respectively. Similar to the case of the argon bubble, there exists a time sequence by which different radicals are produced. Fig. 8(a) shows that the first two species emerging from the reactions are OH• and $HO_2^•$, rather than OH• and H• as in the case of the argon bubble. This suggests a different initiation reaction other than the pyrolysis of water molecules at play in the oxygen bubble. Analysis of the reaction pathway in Fig. 8 (b) identifies this reaction as:

$$O_2 + H_2O \rightarrow 2OH^• + HO_2^• \qquad (R29)$$

The activation temperature of R29 is only about 34813 K compared with the 59700 K for the dissociation of water molecules, suggesting that a much lower energy barrier needs to be overcome in order to trigger the whole chemical reactions in the bubble. Following the activation of the initiation reaction, other reactions occur more readily and begin to produce radicals. This well explains the paradox that more radicals are produced under a milder reaction condition in the oxygen bubble.
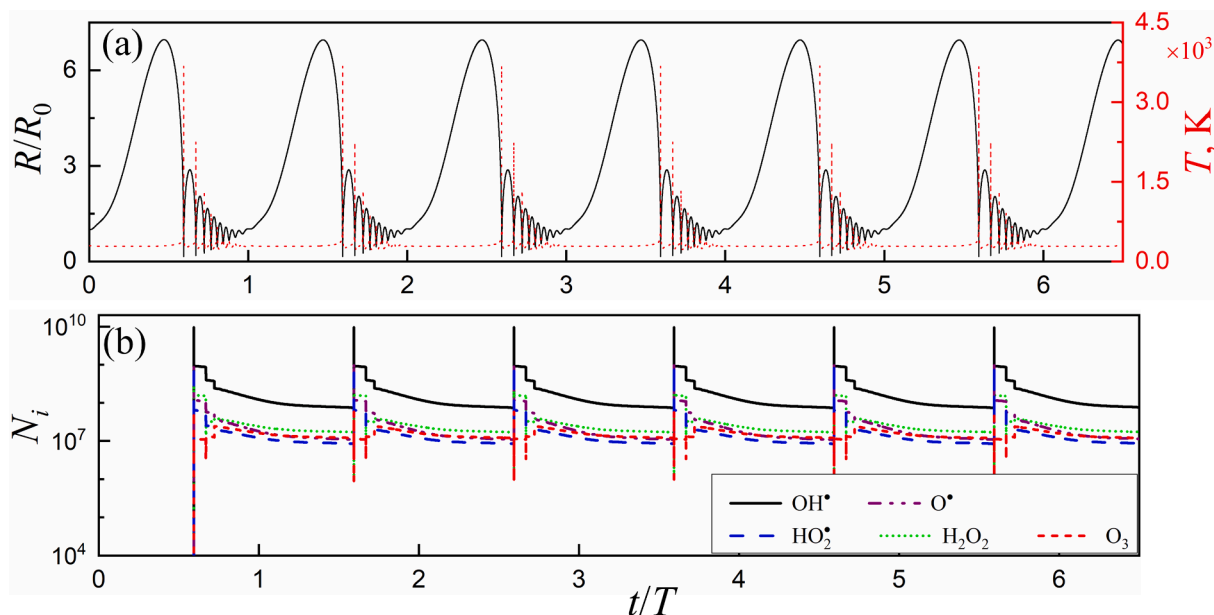
Fig. 7. The bubble dynamics and productions of reactive species inside the oxygen bubble within a period of 6.5 acoustic cycles. (a) Evolution of bubble radius; (b) The temporal variation of the number of particles for the main chemical products. The parameters for the calculated case are: $p_a = 1.3$ bar, $f = 20$ kHz, $R_0 = 10$ μm, and $T_\infty = 298$ K.

The $HO_2^•$ derived from O_2 further reacts with water molecules and produces additional $OH^•$ radicals at later moments as shown in Fig. 8(c).

$$HO_2^• + H_2O \rightarrow H_2O_2 + OH^• \tag{R30}$$

For the $O^•$ atoms, the dissociation of O_2 and the attack of $H^•$ on the O_2 both contribute to its production:

$$O_2 + M \rightarrow 2O^• + M \tag{R31}$$

$$O_2 + H^• \rightarrow O^• + OH^• \tag{R32}$$
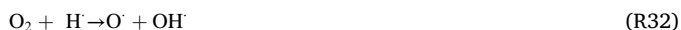
Note that the reaction R32 also produces $OH^•$. In addition, the $O^•$ atoms generated from the pyrolysis of oxygen molecules (R31) provide another production channel for $OH^•$ by combining with water molecules:

$$O^• + H_2O \rightarrow 2OH^• \tag{R33}$$

The reactions R32 and R33 require relatively low activation energies. Therefore, the main constraint for these two reactions is the supply of $O^•$ and $H^•$ atoms. As the collapse progresses and the temperature rises, the $O^•$ and $H^•$ atoms become abundant. In this situation, the production of $OH^•$ through R32 and R33 is accelerated and their contributions increase.

The generation of O_3 is mainly attributed to the attack of $O^•$ on the oxygen molecules:

$$O^• + O_2 \rightarrow O_3 \tag{R34}$$

This reaction is characterized by the high activation energy and its rate at the investigated moment is relatively slow.

Table 5
The production of the main reactive species in the oxygen bubble: $c_{i\text{-max}}$ is the maximum density in mol/m³, $N_{i\text{-max}}$ the peak number of particles inside the bubble at the end of collapse, and $\Delta N_{i\text{-}s}$ the accumulative number of the species dissolved in the liquid during one acoustical cycle.

Species	$OH^•$	$O^•$	$HO_2^•$	H_2O_2	O_3	$H^•$
$N_{i\text{-max}}$	9.4×10^9	9.4×10^8	1.0×10^9	4.6×10^8	5.8×10^7	2.1×10^7
$c_{i\text{-max}}$	1039.0	104.4	112.8	51.1	6.5	2.3
$\Delta N_{i\text{-}s}$	2.9×10^8	4.2×10^7	1.7×10^7	3.4×10^7	1.3×10^7	9.1×10^5

The above reaction mechanism analysis demonstrates that the existence of O_2 in the bubble lowers the energy barrier for radical productions through the initiation reaction R29. This compensates for the adverse effect brought about by the lower collapsing temperature and helps strengthen the efficiency of radical production in the oxygen bubble.

3.2.3. Radical dispersion

The radical dispersion in this case is complicated by the pre-existence of dissolved oxygen in the water that would participate in the chemical reactions. Notably, the combination of the O_2 and the $H^•$ atoms would create $HO_2^•$ radicals through $H^• + O_2 \rightarrow HO_2^•$ (R.6 in Table 3). In addition, the attack of $O^•$ atoms on water molecules may contribute new $OH^•$ radicals via $O^• + H_2O \rightarrow OH^• + OH^•$ (R.13 in Table 3).

Despite these additional reactions, the overall pattern of the radical dissolution at the bubble interface is not changed as can be seen from Fig. 9. The rapid increase and decrease of the main radicals at the bubble surface suggest that the influence of reactions R6 and R13 is not significant due to their small rate constants (see Table. 3). Instead, the robust recombination reactions still dominate the dissolution dynamics and quickly deplete the radicals.

Fig. 10 also suggests that the dispersion characteristics are similar to that in the case of the argon bubble. The radicals react away rapidly within a short diffusion distance. Despite a larger radical supply at the bubble interface, Fig. 10(a) suggests that for $OH^•$ the overall concentration is lower and the penetration depth in the liquid is shorter compared with the case of argon bubble. This is due to the stronger recombination reactions with higher initial concentrations of reactants. The same reason can also explain the diminishing presence of $O^•$ and $HO_2^•$ in the liquid region as displayed in Fig. 10(b) and (c). On the other hand, the initially saturated oxygen in the liquid has indiscernible effects on the radical dispersion. Table. 3 shows that the rate constants for reactions involving molecular oxygen are several orders of magnitude smaller than that for the radical recombination. Therefore, the dispersion behavior of the radicals is predominately driven by the recombination reactions.

In sonochemical degradation of phenol, enhanced treatment efficiency was observed by dissolving oxygen in the solution. There have been conjectures [14] that attribute this phenomenon to the reaction O_2
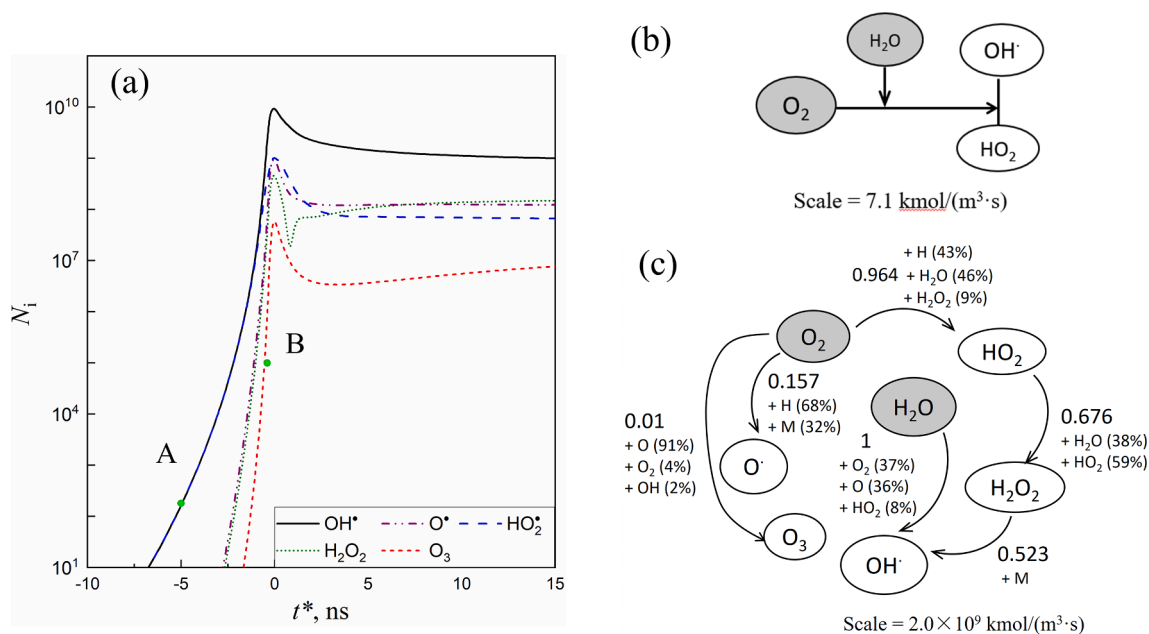
Fig. 8. (a) The productions of radicals in the oxygen bubble around the collapse point. The reaction pathways of O atoms at: (b) t^*=-5 ns when T_b = 1473 K and p_g = 11 MPa, and (c) t^*=-0.4 ns when T_b = 3154 K and p_g = 982 MPa. These two moments are indicated as "A" and "B" in figure (a).

$+ H_2O_2 \rightarrow 2HO_2$ in the liquid phase since it reverts the loss of oxidation potential caused by the recombination of OH radicals. However, The rate constant for this reaction is as low as 4.2×10^{-19} $M^{-1}s^{-1}$ [45,46]. The results from the present simulation show that the effects from such reactions are insignificant. The increased radical production inside the bubble combined with a higher number of bubbles may be responsible.

4. Discussion

The reaction mechanism analysis demonstrates that the production of radicals involves various elementary reactions, among which the initiation reaction is the critical step. It not only produces the main body of the highly reactive OH' radicals, but also influences the productions of other species owing to the nature of chain reactions. The energy barrier of the initiation reaction is an important parameter determining the overall intensity of the radical productions, which in turn is dependent on the initial species of gases inside the bubble. From this perspective, more attention should be paid to the reaction kinetics when discussing the influences of saturated gas on the sonochemical production of radicals.

Our calculation as well as a previous study [10] showed that the number of radicals that diffuse out from the bubble is small compared with the total amount of radicals produced inside the bubble. Therefore, the influence of using different methods to calculate the interfacial flux of radicals, Γ, on the radical production is negligible.

As far as the impact on the radical dispersion is concerned, we tested two approaches to estimating Γ: the uptake method specified by Eq. (4) and the diffusion method dictated by Eq. (5). The simulated OH radicals dissolving at the bubble surface for the argon bubble are depicted in Fig. 11. It shows that while the peak concentration varies between the two methods, the general patterns are similar. Moreover, due to the dominance of recombination reactions in the radical dispersion process, there is no significant difference in the spatial distribution of the radicals, including the penetration distance. It is thus concluded that the specific choice of estimation method for the radical flux doesn't affect the reported results significantly.

Strictly speaking, the liquid layer surrounding the bubble would be heated in the violent collapse as a result of heat diffusion from the interior hotspot. Correspondingly, the exact rates for the reactions in the

radical dispersion simulation should be calculated using the local temperatures. However, for aqueous solutions under room temperatures, a detailed calculation demonstrated that the maximum temperature rise in the liquid layer is on the order of dozens of Kelvins [28]. Therefore, the thermal influence on the reaction rates is expected to be small and all the calculations are based on the ambient temperature in the present simulation. However, the thermodynamic effect is an important feature for cavitation in high-temperature conditions and should be considered in this situation. This involves solving the heat diffusion equation in the liquid region together with the mass diffusion simulation. The numerical method introduced in Section 2.3 can be applied similarly and the grids can be shared as the values of thermal and mass diffusivity are in the same order of magnitude.

The dispersion of radicals in the liquid region is severely constrained by the rapid recombination reactions. The penetration depth of the main radicals OH' is around 0.2 μm and barely changes by the existence of the saturated gas. If the solution contains other scavenging species, this depth is expected to decrease further. This feature may explain the poor performance in some sonochemistry applications. For example, in degrading nonvolatile organic pollutants in wastewater, direct contact between the free radicals and contaminants in the liquid phase is required. The limited sphere of influence of the radicals is the main challenge for fully realizing their oxidation potential. To overcome this inherent deficiency, some strategies have been proposed to drive the pollutants closer to the bubble interface. One of the approaches is adding salts into the solution by altering the partition coefficient of organic pollutants and increasing the concentration at the bubble interface [47]. More studies in this direction are warranted to mitigate the oxidation loss by radical recombinations.

5. Conclusion

In this paper, we propose a complete numerical scheme to integratedly simulate the radical production inside the bubble and dispersion in the outside liquid region. For the former purpose, the bubble dynamics model is coupled with the chemical reaction simulation through the platform Cantera. In the dispersion simulation, the diffusion–reaction equations are solved with the inputs from the production simulation. Two features of practical merits in the proposed model
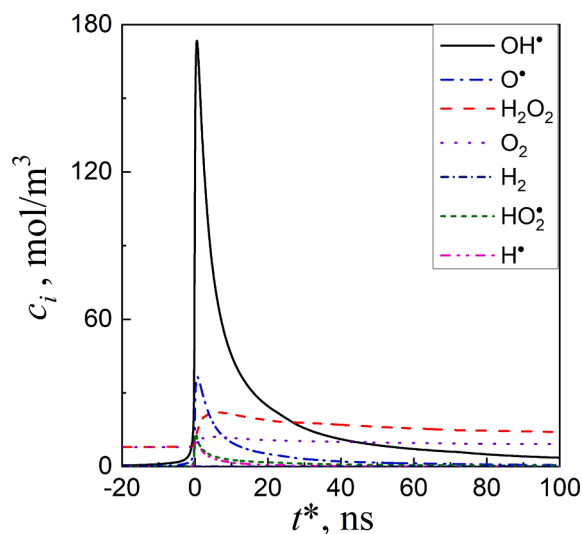
Fig. 9. The dissolution of radicals at the gas–liquid interface ($r = R$) for the oxygen bubble. The concentration of main radicals and recombination products are shown around the collapse ($R = R_{min}$).

have been highlighted: the ability to investigate the production mechanism for each radical species based on reaction pathway analysis, and the ability to reveal the temporal-spatial distribution of the radicals in the liquid phase. To demonstrate the applicability, the typical cases of an argon bubble and an oxygen bubble are investigated with the model. The obtained insights are summarized as follows:

(1) The reactions in the collapsing bubble progress in a cascading way. The production of radicals largely depends on the initiation reaction, which in turn is determined by the initial gas species inside the bubble. Especially, the activation energy of the initiation reaction dictates the overall intensity of the radical productions.

(2) For the argon bubble, the initiation reaction is the thermal dissociation of water molecules and is characterized by the high energy barrier. However, for the oxygen bubble, the reaction between the oxygen molecules and water vapor becomes the initiation step and requires a much lower energy threshold. This explains the enhanced radical productions in the oxygen bubble despite the lower collapsing temperatures.

(3) The dispersion of radicals is strongly driven by the recombination reactions with a penetration distance of smaller than 0.2 μm. Explicit intermittency is noticed in the dispersion behavior in
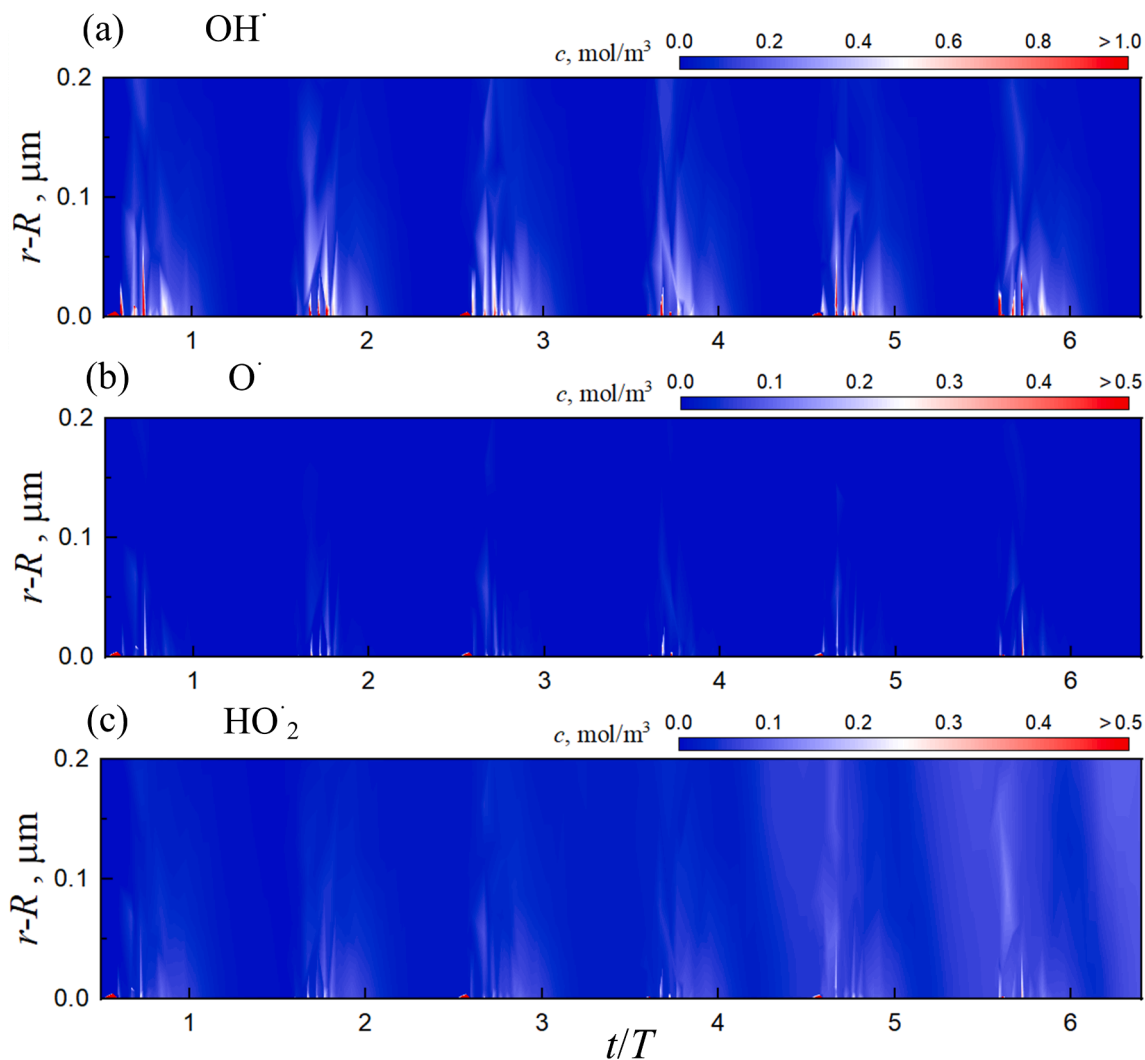

Fig. 10. The dispersion of different radicals in the liquid for the oxygen bubble: (a) OH$^•$ radicals; (b) O$^•$ atoms, and (c) HO$_2^•$ atoms. For the interpretation of the results, the readers are referred to the caption of Fig. 5.
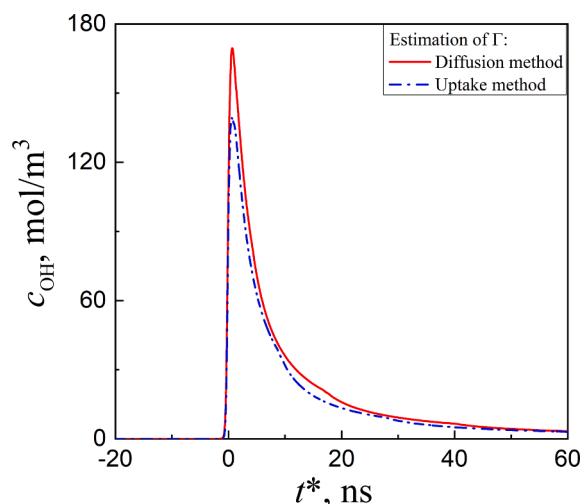
Fig. 11. The influence of the estimation method for the radical flux on the dissolution of OH˙ at the bubble interface for the argon bubble.

response to the periodical collapse of the bubble. In the investigated case, the oxygen initially dissolved in the solution doesn't change the dynamics of dispersion significantly.

Declaration of Competing Interest

The authors declare that they have no known competing financial interests or personal relationships that could have appeared to influence the work reported in this paper.

Acknowledgment

References:

[1] R. Kidak, N.H. Ince, Ultrasonic destruction of phenol and substituted phenols: A review of current research, Ultrasonics Sonochemistry 13 (3) (2006) 195–199.
[2] P. Thanekar, P.R. Gogate, Improved processes involving hydrodynamic cavitation and oxidants for treatment of real industrial effluent, Separation and Purification Technology 239 (2020), 116563.
[3] J.-J. Yao, N.-Y. Gao, C. Li, L. Li, B. Xu, Mechanism and kinetics of parathion degradation under ultrasonic irradiation, Journal of Hazardous Materials 175 (2010) 138–145.
[4] B. Stefanovic, T. Rosenau, A. Potthast, Effect of sonochemical treatments on the integrity and oxidation state of cellulose, Carbohydrate Polymers 92 (2013) 921–927.
[5] K. Kerboua, O. Hamdaoui, Sonochemistry for Water Remediation: Toward an Up-Scaled Continuous Technology, Applied Water Science (2021) 437–467.
[6] B. Flint Edward, S. Suslick Kenneth, T. Temperature, of Cavitation, Science 253 (1991) 1397–1399.
[7] A. Dehane, S. Merouani, Impact of dissolved rare gases (Ar, Xe and He) on single-bubble sonochemistry in the presence of carbon tetrachloride, Chemical Papers 76 (2022) 3011–3030.
[8] A. Dehane, S. Merouani, O. Hamdaoui, M. Ashokkumar, An alternative technique for determining the number density of acoustic cavitation bubbles in sonochemical reactors, Ultrasonics Sonochemistry 82 (2022), 105872.
[9] A. Dehane, S. Merouani, O. Hamdaoui, M.H. Abdellattif, B.-H. Jeon, Y. Benguerba, A full mechanistic and kinetics analysis of carbon tetrachloride (CCl4) sono-conversion: Liquid temperature effect, Journal of Environmental Chemical Engineering 9 (6) (2021) 106555.
[10] K. Yasui, T. Tuziuti, M. Sivakumar, Y. Iida, Theoretical study of single-bubble sonochemistry, The Journal of chemical physics 122 (2005), 224706.
[11] L. Stricker, D. Lohse, Radical production inside an acoustically driven microbubble, Ultrasonics Sonochemistry 21 (2014) 336–345.
[12] C. Kalmár, K. Klapcsik, F. Hegedűs, Relationship between the radial dynamics and the chemical production of a harmonically driven spherical bubble, Ultrasonics Sonochemistry 64 (2020), 104989.
[13] S. Merouani, O. Hamdaoui, Y. Rezgui, M. Guemini, Sensitivity of free radicals production in acoustically driven bubble to the ultrasonic frequency and nature of dissolved gases, Ultrasonics Sonochemistry 22 (2015) 41–50.
[14] T. Sivasankar, V.S. Moholkar, Mechanistic approach to intensification of sonochemical degradation of phenol, Chemical Engineering Journal 149 (2009) 57–69.
[15] M. Kitajima, S.-I. Hatanaka, S. Hayashi, Mechanism of O2-accelerated sonolysis of bisphenol A, Ultrasonics 44 (2006) e371–e373.
[16] J. Rooze, E.V. Rebrov, J.C. Schouten, J.T.F. Keurentjes, Dissolved gas and ultrasonic cavitation – A review, Ultrasonics Sonochemistry 20 (2013) 1–11.
[17] R. Pflieger, T. Chave, G. Vite, L. Jouve, S.I. Nikitenko, Effect of operational conditions on sonoluminescence and kinetics of H2O2 formation during the sonolysis of water in the presence of Ar/O2 gas mixture, Ultrasonics Sonochemistry 26 (2015) 169–175.
[18] M.A. Beckett, I. Hua, Impact of Ultrasonic Frequency on Aqueous Sonoluminescence and Sonochemistry, The Journal of Physical Chemistry A 105 (2001) 3796–3802.
[19] G. Mark, A. Tauber, R. Laupert, H.-P. Schuchmann, D. Schulz, A. Mues, C. von Sonntag, OH-radical formation by ultrasound in aqueous solution – Part II: Terephthalate and Fricke dosimetry and the influence of various conditions on the sonolytic yield, Ultrasonics Sonochemistry 5 (1998) 41–52.
[20] L.B. Ibraguimova, A.L. Sergievskaya, O.P. Shatalov, Dissociation rate constants for oxygen at temperatures up to 11000 K, Fluid Dynamics 48 (2013) 550–555.
[21] P. Maksyutenko, T.R. Rizzo, O.V. Boyarkin, A direct measurement of the dissociation energy of water, The Journal of Chemical Physics 125 (2006), 181101.
[22] F. Gilmore, The growth or collapse of a spherical buble in a viscous compressible liquid, California Institute of Technology, Hydrodynamics Laboratory, Pasadena, California, USA, Report No. 26–4 (1952).
[23] G.P. Smith, D.M. Golden, M. Frenklach, N.W. Moriarty, B. Eiteneer, M. Goldenberg, C.T. Bowman, R.K. Hanson, S. Song, W.C. Gardiner, J. Lissianski, Vitali V., Z. Qin, Gri-mech 3.0., see: http://combustion.berkeley.edu/gri-mech/.
[24] C. Kalmár, T. Turányi, I.G. Zsély, M. Papp, F. Hegedűs, The importance of chemical mechanisms in sonochemical modelling, Ultrasonics Sonochemistry 83 (2022) 105925.
[25] K. Peng, F.G.F. Qin, R. Jiang, W. Qu, Q. Wang, Reactive species created in the collapse of laser-induced cavitation bubbles: Generation mechanism and sensitivity analysis, Journal of Applied Physics 131 (2022), 043101.
[26] S. Kagami, T. Kanagawa, Weakly nonlinear propagation of focused ultrasound in bubbly liquids with a thermal effect: Derivation of two cases of Khokolov–Zabolotskaya–Kuznetsoz equations, Ultrasonics Sonochemistry (2022) 105911.
[27] T. Kanagawa, T. Kamei, Thermal effect inside bubbles for weakly nonlinear pressure waves in bubbly liquids: Theory on short waves, Physics of Fluids 33 (2021), 063319.
[28] L. Stricker, A. Prosperetti, D. Lohse, Validation of an approximate model for the thermal behavior in acoustically driven bubbles, The Journal of the Acoustical Society of America 130 (2011) 3243–3251.
[29] M. Frenklach, H. Wang, M.J. Rabinowitz, Optimization and analysis of large chemical kinetic mechanisms using the solution mapping method—combustion of methane, Progress in Energy and Combustion Science 18 (1992) 47–73.
[30] M.-R. Kalus, N. Bärsch, R. Streubel, E. Gökce, S. Barcikowski, B. Gökce, How persistent microbubbles shield nanoparticle productivity in laser synthesis of colloids–quantification of their volume, dwell dynamics, and gas composition, Physical Chemistry Chemical Physics 19 (2017) 7112–7123.
[31] M.-R. Kalus, R. Lanyumba, N. Lorenzo-Parodi, M.A. Jochmann, K. Kerpen, U. Hagemann, T.C. Schmidt, S. Barcikowski, B. Gökce, Determining the role of redox-active materials during laser-induced water decomposition, Physical Chemistry Chemical Physics 21 (2019) 18636–18651.
[32] D.G. Goodwin, R.L. Speth, H.K. Moffat, B.W. Weber, Cantera: An object-oriented software toolkit for chemical kinetics, thermodynamics, and transport processes, Doi: 10.5281/zenodo.4527812, see: https://www.cantera.org.
[33] J. Jiang, Z. Tan, C. Shan, J. Pan, G. Pan, Y. Liu, X. Chen, X. Wang, A new study on the penetration of reactive species in their mass transfer processes in water by increasing the electron energy in plasmas, Physics of Plasmas 23 (2016), 103503.
[34] W. Tian, M.J. Kushner, Atmospheric pressure dielectric barrier discharges interacting with liquid covered tissue, Journal of Physics D: Applied Physics 47 (2014), 165201.
[35] B.D. Storey, A.J. Szeri, Water vapour, sonoluminescence and sonochemistry, Proc. R. Soc. Lond. A 456 (1999) (2000) 1685–1709.
[36] A. Takami, S. Kato, A. Shimono, S. Koda, Uptake coefficient of OH radical on aqueous surface, Chemical Physics 231 (1998) 215–227.
[37] Y.T. Didenko, K.S. Suslick, The energy efficiency of formation of photons, radicals and ions during single-bubble cavitation, Nature 418 (2002) 394–397.
[38] R. Toegel, D. Lohse, Phase diagrams for sonoluminescing bubbles: A comparison between experiment and theory, The Journal of chemical physics 118 (2003) 1863–1875.
[39] K. Peng, F.G.F. Qin, R. Jiang, S. Kang, Interpreting the influence of liquid temperature on cavitation collapse intensity through bubble dynamic analysis, Ultrasonics Sonochemistry 69 (2020) 105253.
[40] K. Peng, F.G.F. Qin, S. Tian, Y. Zhang, An inverse method to fast-track the calculation of phase diagrams for sonoluminescing bubbles, Ultrasonics Sonochemistry 73 (2021), 105534.

[41] K. Peng, S. Tian, G. Li, Z. Huang, R. Yang, Z. Guo, Bubble dynamics characteristics and influencing factors on the cavitation collapse intensity for self-resonating cavitating jets, Petroleum Exploration and Development 45 (2018) 343–350.

[42] F. Hegedűs, C. Hős, L. Kullmann, Influence of heat transfer on the dynamic response of a spherical gas/vapour bubble, International Journal of Heat and Fluid Flow 31 (2010) 1040–1049.

[43] K.S. Suslick, D.A. Hammerton, R.E. Cline, Sonochemical hot spot, Journal of the American Chemical Society 108 (1986) 5641–5642.

[44] K.S. Suslick, The site of sonochemical reactions, IEEE transactions on ultrasonics, ferroelectrics, and frequency control 33 (1986) 143–147.

[45] B.R. Locke, S.M. Thagard, Analysis and Review of Chemical Reactions and Transport Processes in Pulsed Electrical Discharge Plasma Formed Directly in Liquid Water, Plasma Chemistry and Plasma Processing 32 (2012) 875–917.

[46] S. Mededovic, B.R. Locke, Primary chemical reactions in pulsed electrical discharge channels in water, Journal of Physics D: Applied Physics 40 (2007) 7734–7746.

[47] Y.L. Pang, A.Z. Abdullah, S. Bhatia, Review on sonochemical methods in the presence of catalysts and chemical additives for treatment of organic pollutants in wastewater, Desalination 277 (2011) 1–14.